Chemical Science

ROYAL SOCIETY OF CHEMISTRY

EDGE ARTICLE

View Article Online
View Journal

Cite this: DOI: 10.1039/d6sc01590e

All publication charges for this article have been paid for by the Royal Society of Chemistry

Functional-oriented design of gradient composite fluoride interphase for enhanced silicon anode performance

Yu Jing,[a] Zhixing Wang,[abc] Huajun Guo,[abc] Xinhai Li,[abc] Hui Duan,[abc] Wenjie Peng,[abc] Guochun Yan,[abc] Guangchao Li *[abc] and Jiexi Wang[abc]

Received 25th February 2026
Accepted 18th March 2026

DOI: 10.1039/d6sc01590e

rsc.li/chemical-science

Silicon (Si) is considered a promising next-generation anode due to its ultrahigh theoretical capacity, yet the severe volume changes during cycling that cause interfacial instability and rapid capacity fade remain a major challenge. Conventional fluoride-based interfacial engineering seeks to enhance performance by inducing a LiF-rich SEI, but often overfocuses on LiF content while neglecting the structural and multifunctional requirements of the interphase. Herein, we propose an *in situ* fluorination strategy to construct a composite coating layer comprising crystalline Li_2SiF_6 and amorphous Li_3AlF_6 (denoted as LSAF) on porous silicon (p-Si). This design creates a physicochemical barrier that simultaneously offers high ionic conductivity, superior mechanical strength, and effective electrolyte isolation. The LSAF-1 anode exhibits outstanding cycling stability, retaining 1238.0 mAh g^{-1} after 400 cycles at 2 A g^{-1}. Its advantages are more pronounced under high-temperature and high-rate conditions. Furthermore, it shows remarkable performance in full cells paired with $LiFePO_4$. Mechanistic studies reveal that this coating not only suppresses the accumulation of P/F-containing by-products at the electrode interface but also alleviates volumetric strain by enhancing interfacial mechanical strength. This research provides novel insights for rational interface engineering of Si anodes, advancing the design and development of high-performance anode materials for lithium-ion batteries.

1 Introduction

With the rapid development of electric vehicles and large-scale energy storage systems, the demand for high-energy-density lithium-ion batteries has become increasingly urgent.[1,2] The development of new-generation anode materials with high specific capacity is crucial to achieving this goal.[3,4] Among the candidate materials for next-generation anodes, Si is considered one of the most promising options due to its ultrahigh theoretical specific capacity (~3579 mAh g^{-1} for the $Li_{15}Si_4$ phase), low and safe operating potential, and exceptional natural abundance.[5–7] However, Si experiences dramatic volume changes (>300%) during cycling, which leads to the pulverization of active particles, structural degradation of the electrode, and repeated fracture and reformation of the solid electrolyte interphase (SEI).[8–10] This leads to continuous electrolyte decomposition, irreversible loss of active lithium, and a sharp rise in interfacial impedance, collectively resulting in rapid capacity fading and poor cycling stability, which severely restricts the practical application of Si anodes.[11–13]

To address these challenges, research efforts have primarily focused on two complementary strategies: structural design and interfacial engineering.[14] Structural design, involving nanostructuring, porous design, or composite architectures, aims to accommodate the macroscopic strain associated with volume changes.[15–17] The porous silicon structure, with internal buffering space and short ion-diffusion pathways, enables high capacity and improved cycling stability, making it one of the mainstream solutions for high-performance Si anodes.[18,19] Nevertheless, structural design alone still struggles to resolve the nanoscale dynamic instability at the electrode/electrolyte interface.[20,21] In contrast, interfacial engineering, through surface coating or electrolyte additives, directly targets the construction of a robust and stable interphase, thereby enabling efficient and long-term cycling of Si anodes.[22–24]

Among various interface modification strategies, fluorides have attracted considerable attention due to their unique physicochemical properties.[25,26] Conventional studies focus on fluorides promoting LiF-rich interfaces, but pursuing high LiF content alone is insufficient for silicon anodes.[27] LiF possesses high intrinsic brittleness, making the LiF-rich layer prone to cracking upon repeated volume expansion/contraction of silicon, which exacerbates interfacial instability.[28] Its insulating

[a]School of Metallurgy and Environment, Central South University, 410083 Changsha, China. E-mail: guangchao_li@csu.edu.cn
[b]Engineering Research Center of the Ministry of Education for Advanced Battery Materials, Central South University, Changsha, 410083, China
[c]Hunan Provincial Key Laboratory of Nonferrous Value-Added Metallurgy, Central South University, Changsha, 410083, China

nature also increases impedance when overly thick, hindering rapid Li^+ transport.[29] More importantly, interfacial stability relies on the synergistic effect of multiple SEI components.[30] Solely maximizing LiF content inevitably compromises other functional components, reducing SEI toughness and accelerating failure. Fluoride fast-ion conductors, represented by Li_2SiF_6 and Li_3AlF_6, exhibit high Li^+ conductivity, which can significantly lower the interfacial Li^+ transport barrier and thereby enhance electrode reaction kinetics.[31,32] Moreover, these fast-ion conductors can form a stable interface on the Si surface, effectively suppressing the reductive decomposition of the electrolyte.[31] This "ion transport-mechanical stability" synergistic mechanism transcends the limitation of the traditional coating layer only as a physical barrier, and offers a new direction for the interface design of Si anodes.

Building upon studies on single-component fast-ion conductors, crystalline-amorphous composite structures exhibit unique structural synergistic advantages in interface regulation.[33] The well-ordered crystalline components enhance interfacial structural stability and ion transport efficiency, while the amorphous components offer favorable interfacial compatibility and mechanical flexibility, effectively buffering stress fluctuations induced by volume changes during cycling.[34,35] The integration of these two phases achieves a synergistic "rigid-flexible" effect: the crystalline phase provides mechanical support and ion conduction pathways, whereas the amorphous phase endows the interface with mechanical adaptability and chemical uniformity.[36,37] Furthermore, such multiscale composite structures can induce the formation of a gradient interfacial chemical environment, enabling more precise regulation of lithium-ion flux distribution and suppression of side reactions.[38,39] This provides an ideal structural platform for constructing high-performance SEI layers.

To address the critical challenge that porous silicon structures, while capable of mitigating macroscopic strain, fail to achieve dynamic interfacial stability, this study integrates the intrinsic transport advantages of fast-ion conductors with the design concept of crystalline-amorphous composite architectures. A synergistic fast-ion conductor coating layer composed of crystalline Li_2SiF_6 and amorphous Li_3AlF_6 was successfully constructed on the surface of porous silicon. This design capitalizes on the rapid ion transport pathways of the crystalline phase and the mechanical buffering capability of the amorphous phase, establishing a "physicochemical" barrier that combines high ionic conductivity, excellent mechanical strength, and effective electrolyte isolation. In contrast to conventional strategies that rely on passive protection by thick LiF layers, this coating proactively induces the formation of a thin, dense, and compositionally balanced SEI, thereby suppressing interfacial side reactions at the source. The optimized LSAF-1 electrode exhibits remarkable performance, combining high capacity (2526.9 mAh g^{-1} at 0.2 A g^{-1}) with long cycle life (1238.0 mAh g^{-1} after 400 cycles at 1 A g^{-1}), along with outstanding high-temperature tolerance and Li^+ transport kinetics. This work systematically elucidates the synergistic mechanisms of crystalline-amorphous composite fluoride coatings in terms of chemical regulation, structural support, and kinetic optimization, offering a new paradigm for the rational interface design and performance enhancement of Si anodes.

2 Experimental section

2.1 Materials preparation

2.1.1 Synthesis of p-Si. Typically, commercial $AlSi_{12}$ alloy powder was employed as the precursor in this study. The aluminum component was selectively removed *via* a conventional chemical etching process.[40,41] After the reaction, the product was collected by vacuum filtration and thoroughly washed with deionized water. The porous silicon (p-Si) material was finally obtained after freeze-drying.

2.1.2 Synthesis of p-Si@LSAF. Initially, 0.3 g of p-Si powder was added to 50 mL of ethanol and ultrasonically dispersed for 20 minutes. Subsequently, x mmol LiOH ($x = 0.5$, 1, 1.5 mmol) was dissolved in a mixed solvent consisting of 45 mL ethanol and 5 mL water to prepare a solution. The LiOH solution was added to the porous silicon suspension, and the mixture was stirred for 4 hours. Then, 2 mL of hydrofluoric acid (HF, 50 wt%) was added, and stirring was continued for another 4 hours. The product was collected by filtration, followed by freeze-drying, to obtain the material labeled LSAF-x.

2.2 Materials characterization

The crystal structure parameters of the samples were characterized by X-ray diffractometer (XRD, Empyrean 2, PANalytical) using Cu Kα radiation operated at 40 kV in the 2θ range of 10°–80° with a scanning speed of 10° min^{-1}. The functional groups in the Si-based material were characterized by Fourier Transform-Infrared (FTIR) Spectroscopy (NICOLET iS20, Thermo Fisher Scientific). The scanning electron microscope (SEM, JSM-7900F, JEOL) and transmission electron microscope (TEM, Titan G2 60-300) were employed to observe the morphology and microstructure of the samples, and the element distribution of the material was characterized by the companion X-ray energy dispersive spectrometer (EDS). The chemical composition of materials surface and electrodes SEI layers were investigated by X-ray photoelectron spectroscopy (XPS, Thermo Fisher Scientific) with Al Kα radiation. Thermal gravimetric analyzer (TGA, STA300, HITACHI) was used to characterize the compositions of samples. The atomic force microscopy (AFM) morphology and DMT modulus measurements on the surface of electrodes were performed using a Bruker Dimension Icon instrument. Time-of-flight secondary ion mass spectrometry (TOF-SIMS, PHI Nano TOF 3) analysis was used to analyze the composition and structure of the SEI after cycle. The sputtering rate was set at 25 nm min^{-1} during the measurement.

2.3 Electrochemical tests

The electrochemical performance of the electrodes was evaluated using 2032-type coin cells assembled in an argon-filled glovebox (O_2 < 0.1 ppm, H_2O < 0.1 ppm). The electrode was

prepared by mixing the active material (70 wt%), sodium alginate (20 wt%) and carbon black (10 wt%) with appropriate amount of ethanol and water. The resulting homogeneous slurry was coated onto a copper foil current collector and dried in a vacuum oven at 80 °C for 12 h. The electrode was then punched into discs with a diameter of 12 mm with a mass loading around 0.5 mg cm^{-2}. Lithium metal foil was used as the counter electrode, and the glass microfiber membrane (GF/A) was employed as the separator. The electrolyte was composed of $LiPF_6$ (1 M) in a mixed solution of ethylene carbonate (EC)/diethyl carbonate (DEC) (1 : 1 in volume ratio) with 10 wt% fluoroethylene carbonates (FEC) as the additive. Cyclic voltammetry (CV) was conducted between 0.01 and 2 V with a scan rate of 0.1 mV s^{-1}. Electrochemical cycling tests were performed at 25/45 °C between 0.01 and 2 V. Rate capabilities were tested at 0.2, 0.4, 1, 2, 4, and 0.2 A g^{-1} continuously with 5 cycles per rate. The galvanostatic intermittent titration technique (GITT) was performed in LAND battery test system with 0.2 A g^{-1} lasting for 60 min, followed by a relaxation time of 90 min. The electrochemical impedance spectroscopy (EIS) measurements were carried out on Bio-Logic SP-150 within the frequency range from 10^5 to 10^{-2} Hz with an amplitude of 5 mV. The full cells were assembled by pairing the LSAF-1 with a commercial $LiFePO_4$ (LFP) cathode (active material ratio = 91.5%). The mass loading of cathode was ~12.3 mg cm^{-2}. The N/P ratio of the assembled full cells was controlled around 1.2. The full cells were cycled in the voltage range of 2.0 V to 4.0 V at 0.5 C (1 C = 155 mA g^{-1}). To compensate for the capacity loss during initial cycling, electrochemical pre-lithiation was applied to the Si anodes. First, half-cells comprising the LSAF-1 electrode and a lithium metal electrode were pre-cycled five times within a voltage range of 0.01–2.0 V at 0.2 A g^{-1}. Subsequently, additional lithium was inserted to achieve a pre-lithiation degree of 50% relative to the capacity.

3 Results and discussion

The p-Si@LSAF composite was prepared *via* an *in situ* fluorination strategy (Fig. 1a). Initially, porous silicon (p-Si) was synthesized using a conventional chemical etching method. Subsequently, the p-Si material was added to a LiOH solution under continuous stirring for surface activation, forming

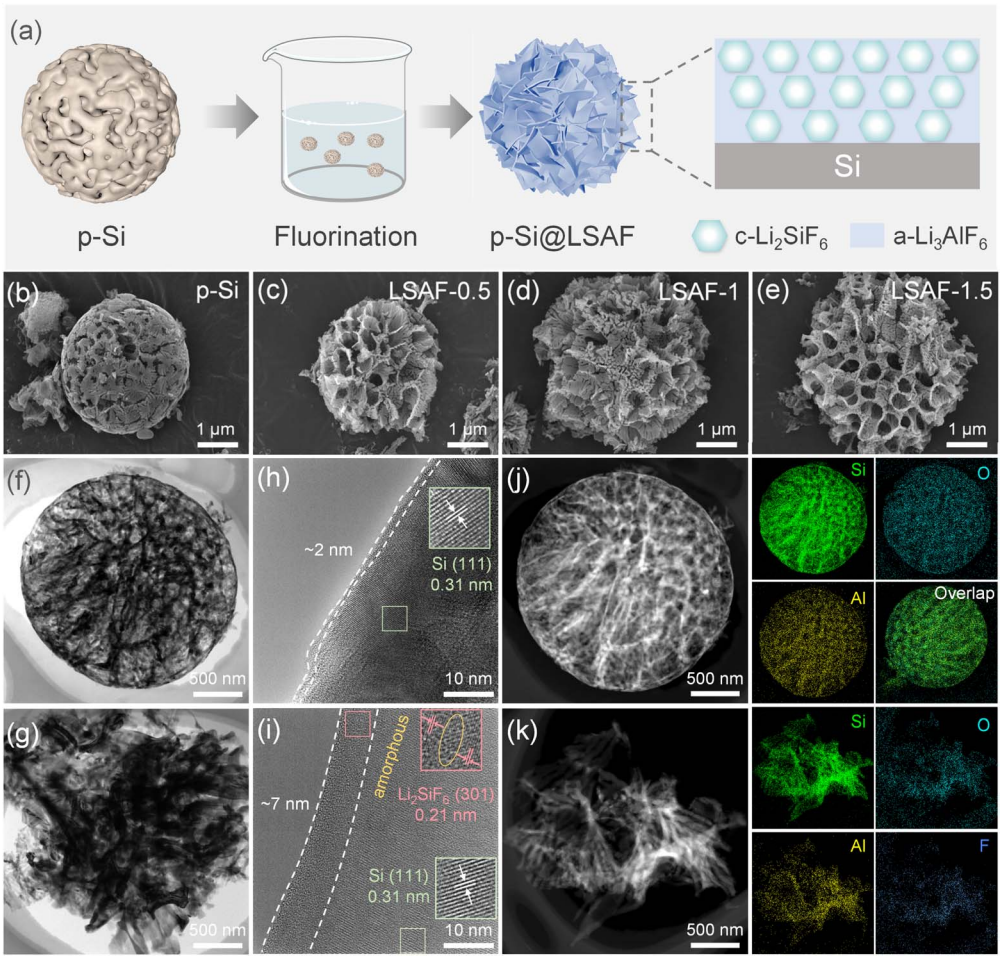

Fig. 1 Morphology and microstructure of the samples. (a) Schematic illustration for the preparation of Si@LSAF. SEM images of (b) p-Si, (c) LSAF-0.5, (d) LSAF-1 and (e) LSAF-1.5. TEM images of (f) p-Si and (g) LSAF-1.5. HRTEM images of (h) p-Si and (i) LSAF-1. Elemental mapping of (j) p-Si and (k) LSAF-1.

a homogeneous suspension. Finally, a HF solution was introduced into the suspension to initiate an *in situ* fluorination reaction on the p-Si surface ultimately yielding the p-Si@LSAF anode material.

Commercial $AlSi_{12}$ microspheres were used as raw material for preparing porous silicon (Fig. S1). Corresponding TEM images reveal the alloy powder consists of solid microspheres, with Al, Si, and O uniformly distributed throughout the material (Fig. S2). To investigate the surface composition of $AlSi_{12}$, XPS characterization was performed (Fig. S3a–c). The O 1s spectrum exhibits peaks corresponding to Al_2O_3 (531.8 eV) and SiO_x (532.9 eV). The Al 2p spectrum exhibits peaks for Al (71.7 and 72.3 eV) and Al_2O_3 (74.4 and 75.6 eV). The Si 2p spectrum exhibited peaks for Si (98.5 and 99.2 eV) and SiO_x (Si^+: 100.6 eV; Si^{2+}: 102.7 eV). The results indicate the presence of a distinct oxide layer on the alloy surface.

The p-Si obtained by chemical etching retained the spherical structural characteristics of the original $AlSi_{12}$ microspheres, with a large number of pores formed on the surface (Fig. 1b). After modification with HF solution, the material underwent a secondary morphological transformation, changing from a "spherical" to a "flower-cluster" morphology, along with a noticeable enlargement of the surface pores (Fig. 1c–e). TEM images reveal the unique hollow, dendritic porous structure of p-Si (Fig. 1f), while LSAF-1 exhibited a porous flower-cluster morphology (Fig. 1g). High-resolution TEM (HRTEM) images indicate that the surface of the p-Si particles is coated with a uniform amorphous layer approximately 2 nm thick (Fig. 1h), whereas the surface of LSAF-1 is covered by a mixed crystalline-amorphous layer about 7 nm thick (Fig. 1i). The crystalline regions display lattice fringes with a spacing of 0.21 nm, corresponding to the (301) plane of Li_2SiF_6. The elemental mappings of p-Si show homogeneous distribution of Al, Si, and O throughout the material (Fig. 1j), indicating that the chemical etching did not completely remove the Al-containing components from the alloy and that a distinct oxide layer was present on the surface, which provided a basis for subsequent *in situ* conversion reactions. Moreover, the uniform distribution of F on the surface of LSAF-1 further confirms the existence of a fluoride coating layer (Fig. 1k).

To determine the material composition, X-ray diffraction (XRD) characterization was performed. The XRD pattern of the $AlSi_{12}$ precursor (Fig. 2a) exhibits strong diffraction peaks corresponding to metallic Al and weaker peaks for Si. After chemical etching, the metallic Al peaks completely disappear, leaving only the characteristic peaks of crystalline Si, indicating that Si becomes the dominant phase after etching. The XRD patterns of the coated materials (Fig. 2b) show the emergence of Li_2SiF_6 diffraction peaks, whose intensity increases with a higher amount of added LiOH. Faint LiF diffraction peaks can also be observed in the pattern of LSAF-1.5. The content of fluoride in the coating layer was determined by thermogravimetric analysis (TGA) under an argon atmosphere. The weight losses for LSAF-0.5, LSAF-1, and LSAF-1.5 are 1.96 wt%, 3.53 wt%, and 12.93 wt%, respectively (Fig. 2c). The onset temperature for this weight-loss process is 245.6 °C, and the temperature corresponding to the maximum rate of mass change is 271.0 °C (Fig. S4). These temperatures are consistent with the reported decomposition temperature of Li_2SiF_6 (approximately 251 °C). The thermal decomposition reaction of Li_2SiF_6 is as follows:

$$Li_2SiF_6 \triangleq 2LiF + SiF_4\uparrow \quad (1)$$

Thus, the mass loss of the materials is attributed to the generation of gaseous SiF_4. The calculated Li_2SiF_6 contents in

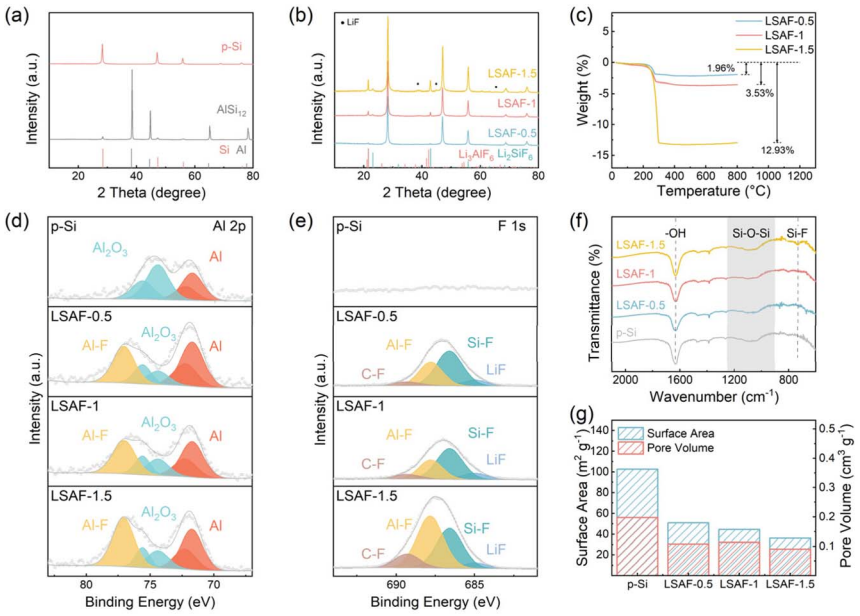

Fig. 2 XRD patterns of (a) $AlSi_{12}$ and p-Si, (b) modified materials. (c) TG curves of the materials with different amounts of coating. (d) Al 2p and (e) F 1s XPS spectra of materials (f) FTIR spectra. (g) Specific surface area and pore volume of materials.

the three samples are 2.94 wt%, 5.29 wt%, and 19.38 wt%, respectively, based on the thermogravimetric data. To investigate the composition of the amorphous phase within the coating layer, the LSAF-1 sample was subjected to heat treatment under an argon atmosphere. After maintaining at 350 °C for 2 hours, the surface Li_2SiF_6 decomposed, leading to an increase in the diffraction peak intensity of LiF. Notably, crystalline Li_3AlF_6 diffraction peaks also appeared simultaneously (Fig. S5a). To clarify the origin of this crystalline Li_3AlF_6—whether it crystallized from pre-existing amorphous Li_3AlF_6 or formed *via* a solid-state reaction between AlF_3 and LiF—the material was heat-treated at a higher temperature. When the temperature was raised to 550 °C, the Li_3AlF_6 peaks intensified, while the LiF peak showed no reduction in intensity (Fig. S5b), indicating that LiF was not significantly consumed in this process. Taken together, these results suggest that the coating layer consists of both crystalline Li_2SiF_6 and amorphous Li_3AlF_6.

To more accurately investigate the surface composition of the materials, X-ray photoelectron spectroscopy (XPS) characterization was performed on each sample. The Al 2p spectrum of p-Si (Fig. 2d) displays two sets of peaks, corresponding to metallic Al (71.7 eV and 72.3 eV) and Al_2O_3 (74.4 eV and 75.6 eV), confirming the presence of residual aluminum in both metallic and oxidized states on the p-Si surface. After the coating process, a new peak attributed to Al–F (77.1 eV) emerges in the Al 2p spectrum of materials, accompanied by a significant decrease in the intensity of the Al_2O_3 peaks. This indicates the conversion of surface Al_2O_3 into Li_3AlF_6. No discernible signal is detected in the F 1s spectrum of p-Si (Fig. 2e), confirming the absence of fluorine-containing species on its surface. In contrast, the F 1s spectrum of the coated materials exhibits characteristic peaks for LiF (685.0 eV), Si–F (686.6 eV), Al–F (687.8 eV), and a trace amount of C–F (689.3 eV), evidencing the successful formation of LiF, Li_2SiF_6, and Li_3AlF_6. The appearance of the C–F signal is likely due to side reactions between hydrofluoric acid and the ethanol solvent. The O 1s spectra of all samples (Fig. S6a) show peaks corresponding to SiO_x (532.9 eV) and Al_2O_3 (531.8 eV). Compared with p-Si, the relative intensity of the SiO_x peak decreases noticeably in the coated materials, suggesting that HF treatment effectively removes part of the surface oxide layer but cannot eliminate it completely. In the Si 2p spectra (Fig. S6b), besides the characteristic peaks of Si (98.5 eV and 99.2 eV), signals corresponding to Si^{4+} (103.3 eV) and Si^{+} (100.6 eV) from SiO_x are observed for all samples. The intensity of the SiO_x peaks diminishes in the coated materials, consistent with the trend observed in the O 1s spectra. To further quantify the effect of HF treatment on surface oxidation, p-Si was treated in an HF solution of the same concentration for 4 hours without adding LiOH. Quantitative analysis reveals that the material oxygen concentration decreases from 9.80 wt% to 4.46 wt% after this treatment (Fig. S7), further confirming that a substantial portion of the oxide layer remains.

To investigate the distribution and evolution of chemical composition within the coating layer along the depth direction, depth-profiling XPS analysis was performed on the LSAF-1 material using Ar^+ sputtering. As Ar^+ etching proceeds, the XPS signals corresponding to surface Al_2O_3 gradually intensify, while those of SiO_x concomitantly weaken (Fig. S8a). Specifically, the signal for the high-valence state Si^{4+} continuously decreases until it vanishes, whereas the signals for the lower-valence states Si^{+} and Si^{2+} progressively increase (Fig. S8b). In the F 1s spectra, the intensity of the signal attributed to Si–F decreases, while that of Al–F slightly increases (Fig. S8c). The evolution of the atomic percentage of each element with sputter time (Fig. S9) shows a trend highly consistent with the aforementioned analysis. These results systematically reveal the multiscale chemical structural evolution of the LSAF-1 material from the surface to the bulk. When transitioning from the outermost surface inward, the coating exhibits a distinct chemical gradient: the uppermost surface is predominantly composed of high-valence-state SiO_x (Si^{4+}) and crystalline Li_2SiF_6. As the etching depth increases, the Al_2O_3 signal progressively strengthens, the chemical state of SiO_x shifts toward lower valence states (Si^{+}/Si^{2+}), and the fluoride composition transitions from being dominated by Li_2SiF_6 toward amorphous Li_3AlF_6. This gradient structure with continuous compositional variation confirms the successful construction of a compositionally graded composite fluoride interphase layer *via* the *in situ* reaction.

The Fourier transform infrared (FTIR) spectra of the materials show a characteristic peak at 1630 cm^{-1}, which is attributed to –OH groups (Fig. 2f). The broad band in the range of 900 to 1300 cm^{-1} corresponds to the vibration of Si–O–Si bonds, indicating the presence of a SiO_x layer on the material surface. Furthermore, in the spectrum of the LSAF-1.5 sample, a characteristic peak at ~730 cm^{-1}, assigned to Si–F bonds, can be observed. The specific surface area and pore structure of the materials were characterized by nitrogen adsorption–desorption measurements (BET) (Fig. 2g, S10 and S11). The specific surface areas of p-Si, LSAF-0.5, LSAF-1, and LSAF-1.5 are 102.5, 50.8, 44.6, and 36.0 $m^2\ g^{-1}$, respectively, while the total pore volumes are 0.198, 0.108, 0.114, and 0.091 $cm^3\ g^{-1}$, respectively. Compared to p-Si, the modified materials exhibit a significant decrease in both specific surface area and pore volume. Notably, the number of mesopores with diameters smaller than 10 nm is markedly reduced. This phenomenon may be attributed to the chemical etching effect of HF during the reaction, which disrupts the original porous framework of the material, leading to partial particle fragmentation and pore collapse, thereby diminishing its porous characteristics.

To evaluate the effects of the porous structure and surface modification layer, systematic electrochemical characterizations were performed on all samples. Fig. 3a displays the initial charge–discharge profiles of different electrodes at 0.2 A g^{-1}. The initial charge specific capacities of the p-Si, LSAF-0.5, LSAF-1, and LSAF-1.5 electrodes are 2673.9, 2654.9, 2526.9, and 2254.0 mAh g^{-1}, respectively, with corresponding initial coulombic efficiencies (ICE) of 83.38%, 84.61%, 85.12%, and 84.99%. Compared with p-Si, the coated materials exhibit a decrease in reversible capacity, which is primarily attributed to the introduction of inactive coating components. Meanwhile, the improved ICE of the coated samples suggests that the constructed synergistic coating layer effectively suppresses side reactions at the electrode/electrolyte interface. Cyclic

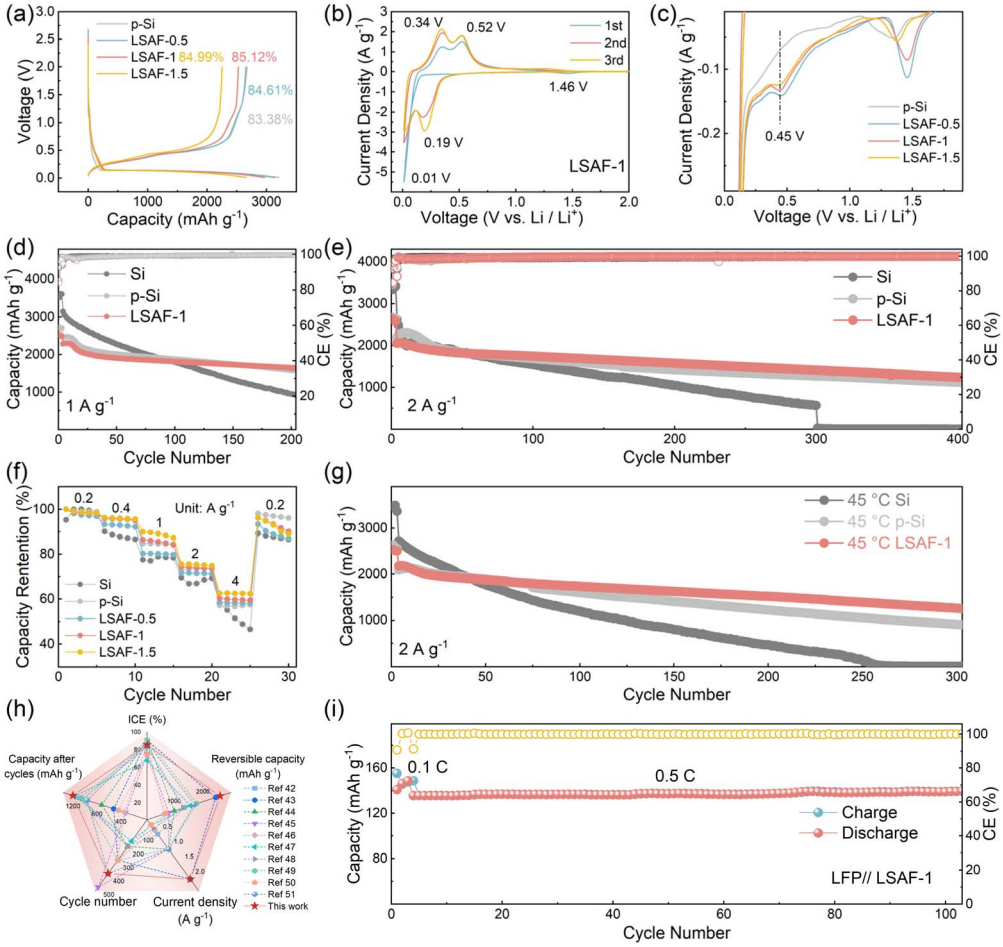

Fig. 3 Electrochemical characterizations of materials. (a) Charge–discharge curves. (b) The CV curve of LSAF-1. (c) Local magnification of the corresponding CV curves. (d) Cycling performance at 1 A g^{-1}. (e) Cycling performance at 2 A g^{-1}. (f) Rate capability from 0.2 to 4 A g^{-1}. (g) Cycling performance at 2 A g^{-1} under 45 °C. (h) Electrochemical performance parameters comparison (i) cycling performance of the LFP//LSAF-1 full cell.

voltammetry (CV) measurements were further conducted within a voltage range of 0.01-2 V (Fig. 3b and S12). For the LSAF-1 electrode, the reduction peak around 1.46 V in the first cycle can be ascribed to irreversible interfacial reactions. In subsequent cycles, the reduction peaks appearing at 0.01 V and 0.19 V correspond to the lithiation process of Si (Li–Si alloy formation), while the oxidation peaks at 0.34 V and 0.52 V correspond to the delithiation process. Compared with p-Si, the polarization voltage of the modified materials is significantly reduced, with LSAF-1 showing the smallest polarization. Moreover, under the influence of the synergistic coating layer, the decomposition voltage of FEC is notably increased, and a new reduction peak emerges at ~0.45 V (Fig. 3c), demonstrating that the coating alters the formation mechanism of the SEI on the electrode surface.

Fig. 3d presents the long-term cycling performance of the samples at a current density of 1 A g^{-1}. The initial charge specific capacities of the Si, p-Si, and LSAF-1 electrodes are 3149.6, 2447.9, and 2289.8 mAh g^{-1}, respectively. After 200 cycles, the corresponding capacity retention rates are 29.7%, 64.4%, and 71.8%. To evaluate the cycling stability under high current rates, extended cycling tests were further conducted at 2 A g^{-1} (Fig. 3e). Under this condition, the initial charge specific capacities of Si, p-Si, and LSAF-1 are 2618.5, 2196.9, and 2054.5 mAh g^{-1}, respectively. Notably, the Si electrode nearly loses all electrochemical activity after 300 cycles, while p-Si and LSAF-1 retain reversible capacities of 1119.5 and 1238.0 mAh g^{-1} after 400 cycles, respectively. These results demonstrate that the synergistic effect between the porous structure and the coating layer significantly enhances the cycling stability of the material. Among the samples with different coating amounts, LSAF-1 exhibits the best cycling performance (Fig. S13 and S14). Furthermore, rate capability tests at various current densities (Fig. 3f) further reveal the electrochemical kinetic advantages imparted by the surface coating layer. The modified electrodes, especially those with higher coating contents, exhibit less capacity decay at high rates, demonstrating that the synergistic coating structure effectively enhances the lithium-ion transport kinetics of the electrode.

Building upon the superior electrochemical performance of LSAF-1 at room temperature, this study further evaluated its cycling stability under an elevated temperature of 45 °C

(Fig. 3g). High temperature tends to exacerbate side reactions at the electrode/electrolyte interface and reduce the reversibility of electrode reactions. Nevertheless, the LSAF-1 electrode achieves an ICE of 79.64%, which is higher than that of the p-Si electrode (77.88%) (Fig. S15). Concurrently, the cycling stability of all electrodes deteriorates at high temperature, with the Si electrode undergoing complete capacity decay after 250 cycles. After 300 cycles, the reversible capacities of the p-Si and LSAF-1 electrodes are 904.2 and 1255.3 mAh g^{-1}, respectively, indicating that the gap in cycling stability between the two materials further widens.

Furthermore, the performance of the LSAF-1 anode was comprehensively compared with other advanced silicon-based anodes reported recently (Fig. 3h).[42–51] The comparative results demonstrate that the LSAF-1 electrode outperforms other modified electrodes in key metrics, including reversible capacity, ICE, and cycling stability, highlighting its considerable potential as a high-performance silicon-based anode material. To evaluate the practical application prospects of the LSAF-1 anode, we assembled CR2032 coin-type full cells by pairing it with a commercial $LiFePO_4$ cathode. The full cell exhibits excellent cycling stability at a rate of 0.5 C (1 C = 155 mA g^{-1}) within a voltage window of 2–4 V (Fig. 3i).

To gain deeper insight into the role of the coating layer in the formation of the SEI, XPS analysis was performed on the electrodes after activation (Fig. S16). In the F 1s spectra (Fig. S16a), the p-Si electrode exhibits characteristic peaks corresponding to LiF (685.0 eV), Si–F (686.6 eV), and P–F (687.8 eV), all of which originate from electrolyte decomposition and interfacial side reactions. In contrast, the signals of all fluorine-containing species are markedly weaker in the LSAF-1 electrode, especially the peak assigned to LiF. The Si 2p spectra of the activated electrodes (Fig. S16b) show peaks from elemental Si (98.8 eV), Li_4SiO_4 (100.2 eV), Li_2SiO_3 (102.1 eV), Si^{4+} (103.3 eV), and Si–F (104.7 eV). The lithium silicates (Li_4SiO_4/Li_2SiO_3) are formed through the conversion of surface SiO_x, which is favorable for Li^+ transport across the interface. Moreover, the stronger signal of elemental Si in the LSAF-1 electrode suggests the formation of a thinner SEI layer on its surface. The P 2p spectra of the electrodes (Fig. S16c) are composed of $Li_xPF_yO_z$ (133.3 eV and 134.4 eV) and P–F (136.6 eV and 137.7 eV), which are mainly derived from electrolyte decomposition. In the LSAF-1 electrode, the intensity of the P-related signals is significantly reduced, indicating suppressed electrolyte decomposition and confirming that the synergistic coating layer effectively enhances the stability of the electrode/electrolyte interface. Quantitative analysis based on the XPS survey spectra of the activated electrodes (Fig. S17) reveals a notable decrease in the atomic percentages of F and P, together with an increase in C and O contents in the LSAF-1 electrode. These results suggest that side reactions at the electrode interface are mitigated and that an SEI layer richer in organic components is formed.

To further elucidate the influence mechanism of the synergistic coating layer on the lithium storage behavior of the electrodes, CV curves of the p-Si and LSAF-1 electrodes were measured at various scan rates (Fig. 4a and b). Based on the CV data, the capacitive contribution ratio of each electrode at different scan rates was further calculated (Fig. 4c and d). As the

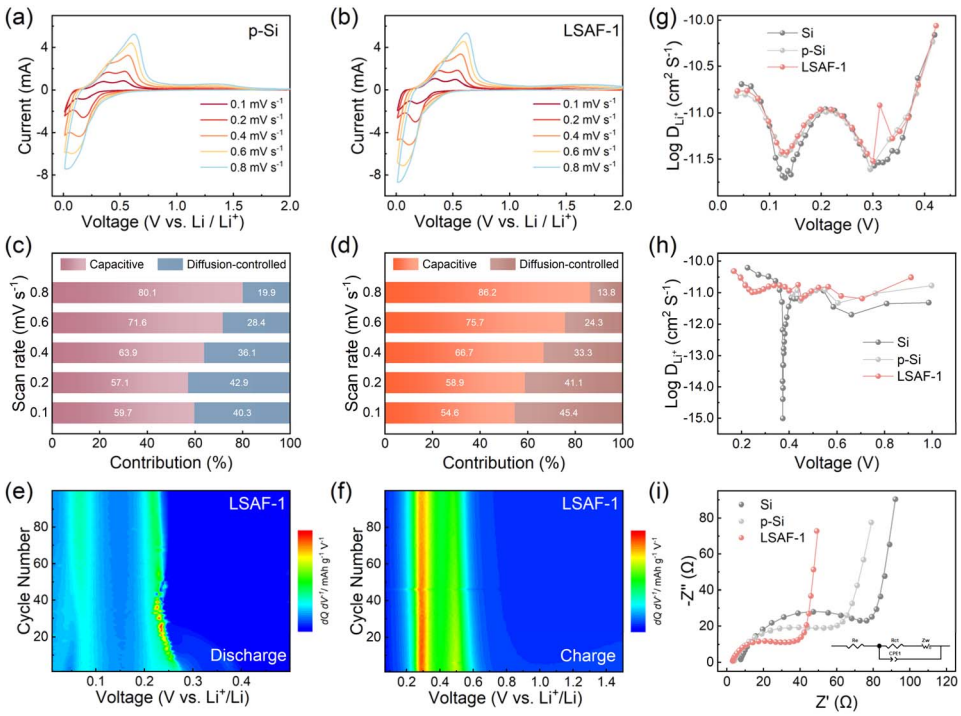

Fig. 4 CV curves of (a) p-Si and (b) LSAF-1 at various scan rates from 0.1 to 0.8 mV s^{-1}. Percentage capacitive contributions of (c) p-Si and (d) LSAF-1 at different scan rates. dQ/dV mappings for the (e) discharging and (f) charging processes of LSAF-1. Corresponding Li^+ diffusion coefficients during (g) discharging and (h) charging progresses. (i) Nyquist plots and fitted curves of electrodes before cycling.

scan rate increases, the proportion of pseudocapacitive contribution rises significantly for both electrodes, and the LSAF-1 electrode consistently exhibits a higher capacitive contribution ratio than p-Si across all scan rates. This difference indicates faster ion diffusion and charge-transfer kinetics in the LSAF-1 electrode, which is mainly attributed to the optimization of the interfacial mass-transport process by the surface composite coating layer. Furthermore, differential capacity curves were analyzed during the initial 100 cycles of the electrodes, with the results presented in Fig. 4e and f. The two cathodic peaks observed during discharge and the two anodic peaks during charge are consistent with the CV results. The contour plot of LSAF-1 shows no obvious peak shift or intensity decay throughout the cycling, indicating low polarization and stable capacity retention. For comparison, the corresponding differential capacity curves of p-Si (Fig. S18a and b) and nano Si (Fig. S18c and d) are also provided. The evolution of the differential capacity curves for the p-Si electrode is similar to that of LSAF-1, yet with weaker lithiation/delithiation peak intensities. In contrast, the lithiation/delithiation peak intensities of the nano Si electrode diminish markedly with cycling, accompanied by significant peak shifts, reflecting severe capacity decay and polarization. These results demonstrate that the LSAF-1 electrode exhibits superior electrochemical performance.

To gain further insight into the Li^+ diffusion behavior, galvanostatic intermittent titration technique (GITT) measurements were performed on the electrodes (Fig. S19a–c). Based on Fick's second law, the Li^+ diffusion coefficients at different voltages were calculated. Notably, the LSAF-1 electrode exhibits higher Li^+ diffusion coefficients during both discharge and charge processes (Fig. 4g and h). Fig. 4i compares the electrochemical impedance spectra (EIS) of the electrodes before cycling to investigate the influence of the composite coating layer on the electrode kinetics. The corresponding impedance parameters were obtained by equivalent circuit fitting (Fig. S20). The results show that both the ohmic resistance ($R_e = 3.0\ \Omega$) and charge-transfer resistance ($R_{ct} = 26.6\ \Omega$) of the LSAF-1 electrode are significantly lower than those of the other electrodes (p-Si: $R_e = 3.6\ \Omega$, $R_{ct} = 45.2\ \Omega$; Si: $R_e = 6.8\ \Omega$, $R_{ct} = 80.0\ \Omega$). These findings clearly demonstrate that constructing a surface composite coating layer can effectively improve the reaction kinetics of the electrode.

To investigate the structure–property relationship between the coating layer and the structural stability of the electrode,

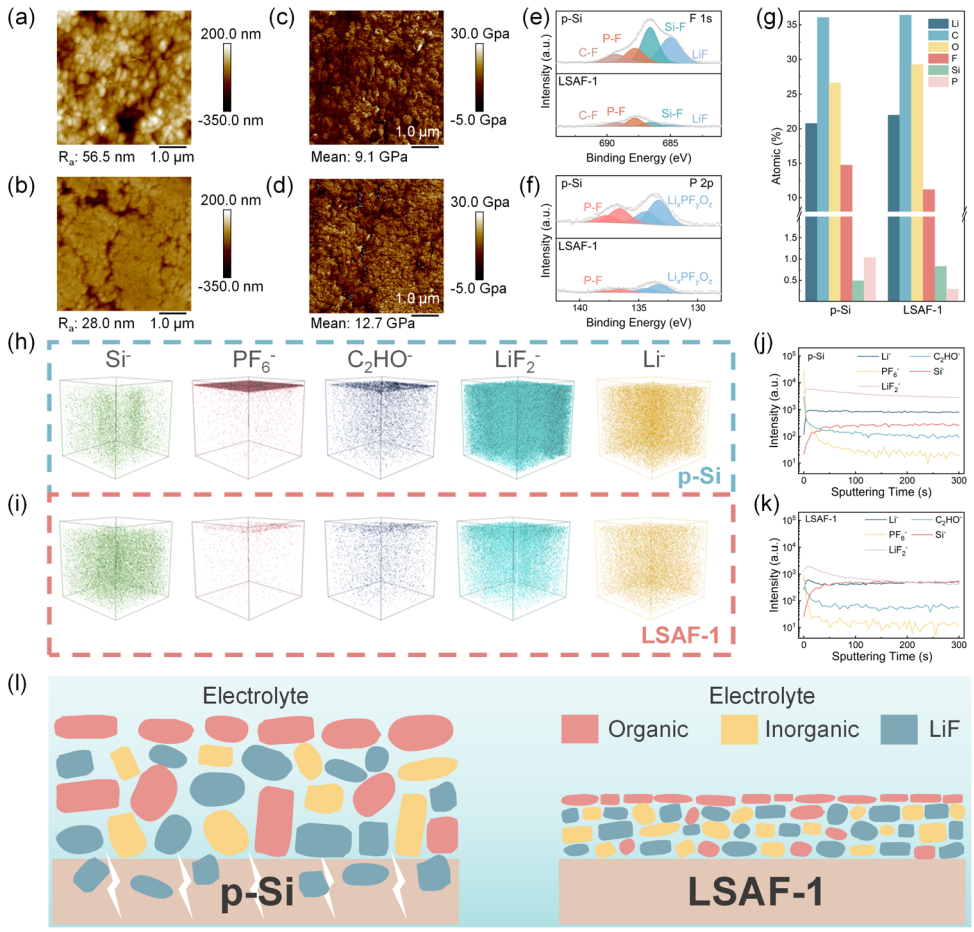

Fig. 5 Comparison of surface roughness of (a) p-Si and (b) LSAF-1 electrodes. 2D plots of DMT modulus of (c) p-Si and (d) LSAF-1 electrodes. (e) F 1s and (f) P 2p XPS spectra for p-Si and LSAF-1 electrodes after cycling. (g) Elemental concentration of the cycled electrode surface. TOF-SIMS 3D renderings of (h) p-Si and (i) LSAF-1 electrodes after cycling. TOF-SIMS sputter depth profiles of key interfacial components in (j) p-Si and (k) LSAF-1 electrodes after cycling. (l) Schematic diagrams of the SEI components of p-Si and LSAF-1 anodes.

quantitative nanomechanical mapping (QNM) atomic force microscopy was employed to characterize different regions of the electrodes after cycling. Surface morphology analysis (Fig. 5a, b and S21a–d) reveals that the LSAF-1 electrode exhibits a significantly lower surface roughness (average value: 23.7 nm) than the p-Si electrode (average value: 53.1 nm), indicating a flatter surface. According to the area distribution of the Derjaguin–Muller–Toporov (DMT) modulus (Fig. 5c, d and S22a–d), the DMT modulus on the LSAF-1 electrode surface (average value: 13.4 GPa) is notably higher than that of the p-Si electrode (average value: 9.3 GPa). This enhancement in mechanical properties primarily stems from the SEI layer induced by the surface modification layer, which possesses higher mechanical strength. Such a high-modulus interface can more effectively accommodate the localized stress generated by Si volume expansion, thereby alleviating issues of particle pulverization and excessive SEI growth.

The macroscopic structural changes of the p-Si and LSAF-1 electrodes before and after cycling were further compared. After 200 cycles, numerous obvious cracks appear on the surface of the p-Si electrode, whereas the LSAF-1 electrode shows fewer and milder cracks (Fig. S23a and b). As shown in Fig. S23c and d, the thicknesses of the p-Si and LSAF-1 electrodes before cycling are 12.0 μm and 13.6 μm, respectively. After 200 cycles, the thickness of the p-Si electrode increases to 39.2 μm, corresponding to a volume expansion of 227%, while the thickness of the LSAF-1 electrode increases only to 31.1 μm, with a volume expansion rate of 129%. These results demonstrate that the surface modification strategy adopted in this work effectively suppresses the overall volume expansion of the electrode.

To investigate the influence of the surface modification layer on the dynamic evolution of SEI components during cycling, XPS characterization was performed on the cycled electrodes. In the F 1s spectra (Fig. 5e), all electrodes exhibit characteristic peaks of LiF, Si–F, and P–F. In the P 2p spectra (Fig. 5f), peaks corresponding to $Li_xPF_yO_z$ and P–F are observed. Notably, the signal intensities of P-containing species are significantly weaker in the LSAF-1 electrode, providing direct evidence that the constructed coating layer effectively suppresses the decomposition of $LiPF_6$ during cycling. Furthermore, the synchronous attenuation of Si–F bond signals indicates that the modification layer inhibits the intrinsic side reactions between Si and the electrolyte. Crucially, the corresponding decrease in LiF signals reveals a non-conventional interface stabilization mechanism. Instead of relying solely on the generation of a LiF-rich SEI, the coating layer establishes a robust physicochemical barrier that fundamentally mitigates interfacial failure by reducing the excessive formation of LiF from electrolyte decomposition and side reactions. This finding challenges the traditional view that "a LiF-rich SEI is optimal," suggesting a new paradigm for interfacial stabilization. Quantitative analysis of the XPS survey spectra of the cycled electrodes (Fig. 5g) shows a decrease in the atomic percentages of F and P, along with a relative increase in Si content in the coated material. This indicates that side reactions at the electrode interface are effectively suppressed, leading to the formation of a thinner and more stable SEI layer.

Cycling at elevated temperature (45 °C) exacerbates the complexity of side reactions at the electrode/electrolyte interface. Surface topography analysis visually reveals the differences in interfacial stability among the electrodes under high-temperature conditions. The p-Si electrode surface exhibits a rough morphology covered with coarse particles (Fig. S24a), which are typical manifestations of excessive SEI growth and structural looseness. In contrast, protected by the coating layer, the LSAF-1 electrode maintains a relatively smooth and compact surface morphology (Fig. S24b). This observation aligns with its superior cycling stability at high temperature, providing visual evidence that the coating layer effectively suppresses high-temperature interfacial degradation. Surface XPS analysis further elucidates the interfacial regulation mechanism of the coating layer. The F 1s spectra show a simultaneous reduction in the signals corresponding to both Si–F and LiF components in the LSAF-1 electrode (Fig. S24c and d), offering direct evidence for the synergistic effect of physical barrier and chemical passivation provided by the coating layer. Specifically, the coating layer can induce the formation of SEI components with higher chemical stability while effectively isolating direct contact between the active Si and the electrolyte, thereby significantly inhibiting their intrinsic side reactions.

To gain deeper insight into the chemical composition and spatial distribution of the electrode interface, time-of-flight secondary ion mass spectrometry (TOF-SIMS) characterization was performed on the cycled electrodes. Three-dimensional distribution maps of various secondary ion species (Fig. 5h and i) and corresponding sputtering depth profiles (Fig. 5j and k) were obtained. In the TOF-SIMS signals, Si^- originates from the active Si material; PF_6^- and C_2HO^- represent decomposition products of the lithium salt and organic solvent, respectively; LiF_2^- indicates the inorganic component LiF; while the distribution of Li^- reveals the accumulation of inactive lithium. The results show that a thin interfacial layer rich in LiF but with minimal organic impurities forms on the surface of the LSAF-1 electrode. Toward the interior, the signal is dominated by active Si^-, whereas signals from side-reaction-derived LiF_2^- and inactive Li^- remain at low levels. In contrast, the SEI surface of the p-Si electrode is enriched with organic by-products (PF_6^- and C_2HO^-), while high concentrations of LiF_2^- and inactive Li^- are diffusely distributed throughout the entire electrode. The sputtering depth profiles further corroborate this trend. HRTEM images of the cycled electrodes further reveal distinct interfacial architectures (Fig. S25a and b). In stark contrast to the p-Si electrode, a thinner and more uniform SEI layer is observed on the LSAF-1 electrode. Such an interfacial architecture is beneficial for fast lithium-ion transport and long-term structural stability.

Benefiting from the regulation of the surface coating layer, the LSAF-1 electrode forms a distinct bilayer structure characterized by "LiF-enriched surface and clean interior," effectively confining side reactions to a shallow surface region (Fig. 5l). In comparison, the p-Si electrode exhibits substantial accumulation of organic by-products on the surface, along with widespread distribution of high-concentration LiF and dead Li throughout the electrode bulk, confirming the continuous

occurrence and deep penetration of interfacial side reactions during cycling. This comparison indicates that merely pursuing a high chemical proportion of LiF in the SEI cannot ensure long-term interfacial stability, suggesting that an interface strategy relying solely on LiF-rich chemistry without structural design has inherent limitations.

4 Conclusions

In summary, this study successfully constructed a Li_2SiF_6/Li_3AlF_6 composite fluoride coating layer on the surface of p-Si, realizing a function-oriented interfacial engineering strategy. This composite layer not only acts as a physical barrier but also chemically guides the formation of a SEI with excellent mechanical strength and high ionic conductivity. The resulting bilayer interface structure—characterized by a LiF-enriched surface and a clean interior—effectively confines side reactions to a shallow surface region, significantly enhancing the long-term cycling stability of the interface. Systematic electrochemical evaluations demonstrate that the optimized LSAF-1 electrode exhibits outstanding cycling stability, high ICE, remarkable rate capability, and good tolerance under elevated temperature conditions. Both interfacial kinetics and mechanical stability are substantially improved. This work breaks through the limitation of traditional interfacial engineering that merely pursues high LiF content, highlighting the importance of synergistic optimization among structural design, mechanical properties, and chemical functionality of the interface layer. The study not only deepens the understanding of the interfacial failure mechanisms in silicon-based anodes but also provides new design principles and theoretical foundations for the development of next-generation high-energy-density lithium-ion battery anode materials and their interfacial engineering.

Declaration of generative AI and AI-assisted technologies in the writing process

During the preparation of this manuscript, the authors used DeepSeek-V3 to improve its spelling, grammar, clarity and overall readability. After using these tools or services, the authors reviewed and edited the content as needed and take full responsibility for the content of the publication.

Author contributions

Yu Jing: conceptualization, formal analysis, investigation, methodology and writing – original draft. Zhixing Wang: methodology, resources, supervision and writing – review & editing. Huajun Guo: methodology, validation. Xinhai Li: investigation, resources. Hui Duan: data curation, formal analysis and visualization. Wenjie Peng: methodology, resources. Guochun Yan: formal analysis, methodology. Guangchao Li: data curation, formal analysis, methodology, supervision, validation and writing – review & editing. Jiexi Wang: conceptualization, data curation, supervision and writing – review & editing.

Conflicts of interest

There are no conflicts to declare.

Data availability

The data that support the findings of this study are available within the article and its supplementary information (SI). Supplementary information: morphology, structure, oxygen content and spectroscopic characterization of materials; XPS spectra, AFM, SEM and TEM images of electrodes; long-term cycling performance of half cells at 1 and 2 A g^{-1}; dQ/dV mappings, CV and GITT curves of electrodes. See DOI: https://doi.org/10.1039/d6sc01590e.

Acknowledgements

We thank the support from the Natural Science Foundation of China (22178394, 52404332, U24A2099), the Science and Technology Innovation Program of Hunan Province (2022RC3048), National Sustainable Development Innovation Demonstration Zone Construction Project (2023sfq63).

References

1 J. Park, J. Kim, J. Kim, M. Kim, T. Song and U. Paik, *Chem. Sci.*, 2025, **16**, 6598–6619.
2 M. M. Hasan, R. Haque, M. I. Jahirul, M. G. Rasul, I. M. R. Fattah, N. M. S. Hassan and M. Mofijur, *J. Energy Storage*, 2025, **120**, 116511.
3 B. Zhu, X. Wang, P. Yao, J. Li and J. Zhu, *Chem. Sci.*, 2019, **10**, 7132–7148.
4 W. He, W. Xu, Z. Li, Z. Hu, J. Yang, G. Qin, W. Teng, T. Zhang, W. Zhang, Z. Sun and X. Yu, *Adv. Sci.*, 2025, **12**, 45.
5 M. Li, S. Li, D. Yan, Y. Ma, X. Niu and L. Wang, *Chem. Sci.*, 2025, **16**, 2609–2618.
6 Z. He, C. Zhang, Z. Zhu, Y. Yu, C. Zheng and F. Wei, *Adv. Funct. Mater.*, 2024, **34**, 2408285.
7 N. Kim, Y. Kim, J. Sung and J. Cho, *Nat. Energy*, 2023, **8**, 921–933.
8 L. Sun, Y. Liu, L. Wang and Z. Jin, *Adv. Funct. Mater.*, 2024, **34**, 2403032.
9 Z. Xiao, H. Wu, L. Quan, F. Zeng, R. Guo, Z. Ma, X. Chen, J. Zhan, K. Xu, L. Xing and W. Li, *Energy Environ. Sci.*, 2025, **18**, 4037–4052.
10 M. Khan, S. Yan, M. Ali, F. Mahmood, Y. Zheng, G. Li, J. Liu, X. Song and Y. Wang, *Nano-Micro Lett.*, 2024, **16**, 179.
11 L. Yang, S. Li, Y. Zhang, H. Feng, J. Li, X. Zhang, H. Guan, L. Kong and Z. Chen, *J. Energy Chem.*, 2024, **97**, 30–45.
12 Y. Li, Z. Cao, Y. Wang, L. Lv, J. Sun, W. Xiong, Q. Qu and H. Zheng, *ACS Energy Lett.*, 2023, **8**, 4193–4203.
13 W. Li, S. Xu, C. Zhong, Q. Fang, S. Weng, Y. Ma, B. Wang, Y. Li, Z. Wang and X. Wang, *Nano-Micro Lett.*, 2025, **17**, 322.

14 M. Je, D.-Y. Han, J. Ryu and S. Park, *Acc. Chem. Res.*, 2023, **56**, 2213–2224.
15 L. Shen, K. Sun, F. Xi, Z. Jiang, S. Li, Y. Wang, Z. Tong, J. Lu, W. Ma, M. A. Green and X. Hao, *Energy Environ. Sci.*, 2025, **18**, 4348–4361.
16 H. Li, H. Li, Y. Lai, Z. Yang, Q. Yang, Y. Liu, Z. Zheng, Y. Liu, Y. Sun, B. Zhong, Z. Wu and X. Guo, *Adv. Energy Mater.*, 2022, **12**, 2102181.
17 Z. Sun, Z. Zhang, S. Zhou, W. Liu, J. Liu, Q. Yin, J. Pan, X. Wu, Z. Zhuang, D.-L. Peng and Q. Zhang, *J. Materiomics*, 2025, **11**, 101053.
18 Z. Cheng, H. Jiang, X. Zhang, F. Cheng, M. Wu and H. Zhang, *Adv. Funct. Mater.*, 2023, **33**, 2301109.
19 Z. Han, P. Maitarad, N. Yodsin, B. Zhao, H. Ma, K. Liu, Y. Hu, S. Jungsuttiwong, Y. Wang, L. Lu, L. Shi, S. Yuan, Y. Xia and Y. Lv, *Nano-Micro Lett.*, 2025, **17**, 200.
20 Y. Yu, C. Yang, Y. Jiang, Z. Shang, J. Zhu, J. Zhang and M. Jiang, *Adv. Energy Mater.*, 2025, **15**, 2403086.
21 Y. Jing, G. Li, Z. Wang, X. Li, W. Peng, H. Guo, H. Duan, G. Yan and J. Wang, *ACS Appl. Mater. Interfaces*, 2024, **16**, 67803–67812.
22 H. Zhang, K. Tao, X. Zeng, C. Chen, Y. Zhu, T. Han, J. Li and J. Liu, *Chem. Sci.*, 2024, **15**, 15769–15775.
23 Z. Sun, Q. Yin, S. Zhou, H. Chen, S. Wen, H. Yang, X. Wu, J. Pan, J. Han, H. Yang, Z. Zhuang, S. Feng, L. Zhang, D.-L. Peng and Q. Zhang, *Adv. Energy Mater.*, 2025, **15**, 2500189.
24 Y. Gao, K. Zhang, X. Du, G. Liu, Y. Du and J. Li, *Chem.–Eng. J.*, 2025, **508**, 160846.
25 J. Sun, L. Lv, Y. Li, Y. Wang, L. Wang, W. Xiong, L. Huang, Q. Qu and H. Zheng, *Angew. Chem., Int. Ed.*, 2025, **64**, e202507688.
26 W. Kang, M. Je, S. Park and C. Jo, *Chem.–Eng. J.*, 2026, **528**, 172605.
27 J. Fang, K. Wu, L. Qin, J. Li, A. Li and H. Feng, *J. Colloid Interface Sci.*, 2025, **679**, 819–829.
28 Z. Li, L. Wang, X. Huang and X. He, *Small*, 2024, **20**, 2305429.
29 J. Tan, J. Matz, P. Dong, J. Shen and M. Ye, *Adv. Energy Mater.*, 2021, **11**, 2100046.
30 Y. Gao and B. Zhang, *Adv. Mater.*, 2023, **35**, 2205421.
31 K. Zhang, J. Zhong, B. Yan, B. Xia and J. Li, *ACS Appl. Nano Mater.*, 2024, **7**, 8053–8062.
32 R. Miyazaki, G. Yamaguchi, E. Yagi, T. Yoshida and T. Tomita, *ACS Appl. Energy Mater.*, 2024, **7**, 2533–2541.
33 K. Hu, J. Zhang, X. Yu, J. Wang and X. Hu, *Energy Environ. Sci.*, 2025, **18**, 7882–7893.
34 X. Zhu, S. Xia, H. Zheng, Y. Shi, X. Zhang, K. Liu, Z. Zhou, Z. Zhai, Y. Fu, Q. Wei, C. Wang, W. Chen, W. Yang and R. Yu, *Energy Storage Mater.*, 2026, **86**, 104939.
35 X. Fu, J. Wu, Z. Zhou, M. J. Tan, Y. Huang, J. Sun, W. Song, P. Guan, Y. Yang, Y. Li and R. O. Ritchie, *Acta Mater.*, 2025, **287**, 120787.
36 H. Lan, J. Wang, L. Cheng, D. Yu, H. Wang and L. Guo, *Chem. Soc. Rev.*, 2024, **53**, 684–713.
37 M. Liu, H. Su, X. Liu, X. He, P. Tan, F. Liu and J. Pan, *Nat. Commun.*, 2025, **16**, 2826.
38 L. Ma, Y. Fang, N. Yang, N. Li, L. Chen, D. Cao, Y. Lu, Q. Huang, T. Song, Y. Su and F. Wu, *Adv. Mater.*, 2024, **36**, 2404360.
39 H. Ren, Y. Yang, C. Lu, X. Ma and Y. Li, *Adv. Funct. Mater.*, 2026, e32199.
40 K. Zhang, X. Gu, X. Jiang, L. Cui and J. Yang, *Mater. Today Commun.*, 2024, **39**, 109004.
41 K.-C. Chang, T. A. N. Bui, R. Niu, Y.-S. Chen and Y.-S. Su, *J. Energy Storage*, 2024, **96**, 112597.
42 J. Cao, X. Yan, D. Li, L. Hu, T. Chen, W. Gao, W. Song, X. Xia, Y. Xia, W. Zhang and H. Huang, *Chem.–Eng. J.*, 2025, **504**, 159049.
43 Y. Dong, D. An, F. Li, H. Jin, B. Li, X. Ma, M. Yao, Z. Yang and F. Yuan, *ACS Nano*, 2025, **19**, 28383–28396.
44 X. Nie, G. Wei, C. Zhang, F. Ji, T. Bai, W. Xia, J. Gao, Y. Wang, W. Zhai, J. Lu, D. Li and L. Ci, *Small*, 2025, **21**, e09098.
45 Z. Yang, K. Zhang, H. Wang, L. Zhu, X. Du and J. Li, *Chem.–Eng. J.*, 2025, **526**, 171120.
46 H. Tong, M. Zhong, H. Xu, Z. An, W. Shen, J. Zhang and S. Guo, *ACS Appl. Mater. Interfaces*, 2025, **17**, 65577–65589.
47 W. Xu, Z. Sun, C. Tang, Z. Cheng, W. Sun, A. Du, Q. Zhang, M. Wu and H. Zhang, *Adv. Funct. Mater.*, 2025, **35**, 2422743.
48 Y.-H. Lee, B.-S. Kim, I.-C. Choi and C.-M. Park, *ACS Nano*, 2025, **19**, 41200–41212.
49 Z. Liu, S. Wang, M. Zheng, Y. Zhang, R. Yu, X. Chen, W. Xiong, Z. Xu, Z. Zhuang, Y. Xia and L. Shen, *Adv. Mater.*, 2026, **38**, e17989.
50 W. Lai, J. H. Lee, Z. Y. Yeo, Y. Yuan, Y. Liu, L. Shi, Y. Pu, Y. K. Ong, C. M. A. Limpo, Y. Rao, T. Xiong, M. Lanza, N. D. Loh and B. Özyilmaz, *ACS Nano*, 2025, **19**, 38040–38052.
51 X. Xue, B. Lou, W. Pang, S. Han, J. Zhang, J. Wu, L. Tian, N. Shi and D. Liu, *Carbon*, 2025, **238**, 120255.